Geochemistry Geophysics Geosystems G3
AN ELECTRONIC JOURNAL OF THE EARTH SCIENCES
Published by AGU and the Geochemical Society

Technical Brief
Volume 10, Number 8
27 August 2009
Q08019, doi:10.1029/2009GC002391
ISSN: 1525-2027

Click Here for Full Article

LitMod3D: An interactive 3-D software to model the thermal, compositional, density, seismological, and rheological structure of the lithosphere and sublithospheric upper mantle

J. Fullea
Group Dynamics of the Lithosphere, Institute of Earth Sciences J. Almera, CSIC, E-08028 Barcelona, Spain (jfullea@ija.csic.es)

J. C. Afonso
Group Dynamics of the Lithosphere, Institute of Earth Sciences J. Almera, CSIC, E-08028 Barcelona, Spain

Now at ARC National Key Centre for the Geochemical and Metallogenic Evolution of Continents, Department of Earth and Planetary Sciences, Macquarie University, North Ryde, New South Wales 2109, Australia.

J. A. D. Connolly
Earth Sciences Department, ETH Zurich, Soneggstrasse 5, CH-8092 Zurich, Switzerland

M. Fernàndez and D. García-Castellanos
Group Dynamics of the Lithosphere, Institute of Earth Sciences J. Almera, CSIC, E-08028 Barcelona, Spain

H. Zeyen
Interactions et Dynamique des Environnements de Surface, UMR 8146, Département des Sciences de la Terre, Université Paris-Sud 11, Bâtiment 504, F-91504 Orsay CEDEX, France

[1] We present an interactive 3-D computer program (LitMod3D) developed to perform combined geophysical-petrological modeling of the lithosphere and sublithospheric upper mantle. In contrast to other available modeling software, LitMod3D is built within an internally consistent thermodynamic-geophysical framework, where all relevant properties are functions of temperature, pressure, and composition. By simultaneously solving the heat transfer, thermodynamic, rheological, geopotential, and isostasy (local and flexural) equations, the program outputs temperature, pressure, surface heat flow, density (bulk and single phase), seismic wave velocities, geoid and gravity anomalies, elevation, and lithospheric strength for any given model. These outputs can be used to obtain thermal and compositional models of the lithosphere and sublithospheric upper mantle that simultaneously fit all available geophysical and petrological observables. We illustrate some of the advantages and limitations of LitMod3D using synthetic models and comparing our predictions with those from other modeling methods. In particular, we show that (1) temperature at midlithosphere depths may be overestimated by as much as 200 K when compositional heterogeneities in the mantle and T-P effects are not considered in lithospheric models and (2) the neglect of mantle phase transformations on gravity-based models in thin-crust settings can result in a significant overestimation and underestimation of the derived crustal thickness and its internal density distribution, respectively.

Components: 10,083 words, 11 figures, 1 table.

Keywords: lithsopheric modeling; mantle composition; potential fields; seismic velocities; thermal modeling.

Index Terms: 0545 Computational Geophysics: Modeling (4255); 1212 Geodesy and Gravity: Earth's interior: composition and state (7207, 7208, 8105, 8124); 1213 Geodesy and Gravity: Earth's interior: dynamics (1507, 7207, 7208, 8115, 8120).

Received 21 January 2009; **Revised** 21 May 2009; **Accepted** 24 June 2009; **Published** 27 August 2009.

Fullea, J., J. C. Afonso, J. A. D. Connolly, M. Fernàndez, D. García-Castellanos, and H. Zeyen (2009), LitMod3D: An interactive 3-D software to model the thermal, compositional, density, seismological, and rheological structure of the lithosphere and sublithospheric upper mantle, *Geochem. Geophys. Geosyst.*, *10*, Q08019, doi:10.1029/2009GC002391.

1. Introduction

[2] One of the main challenges concerning the Earth's upper mantle is the determination of its present-day thermal and compositional structure. This information represents the basis for any evolutionary model of the Earth, as well as for understanding the relationships between geophysical observables (e.g., gravity, seismic velocity) and the physical state of the Earth's interior. The existence of regions where temperature and composition vary abruptly within the lithospheric mantle is now generally accepted, as well as their spatial association with the location of seismically active zones, ore deposits, seismic velocity anomalies, sedimentary basins, and major tectonic boundaries in general [*Fouch et al.*, 2004; *Carlson et al.*, 2005; *Shomali et al.*, 2006; *Levshin et al.*, 2007; *Griffin et al.*, 2009]. Realistic thermal and compositional models of the lithosphere and sublithospheric upper mantle are therefore essential for understanding (1) the origin and evolution of the lithosphere, (2) the nature of the lithospheric/sublithospheric mantle coupling, (3) the relationship between surface features and deep seated processes, and (4) the emplacement of major ore deposits, among others. However, given the trade-offs between temperature and composition, neither potential fields nor seismic velocities alone are sufficient to put tight constraints on the thermal and compositional structures of the upper mantle.

[3] The purpose of this paper is to present an interactive 3-D software (referred to as LitMod3D) intended for integrated geophysical-petrological modeling of the upper mantle and to make it available to community modelers. LitMod3D implements an updated version of the recent method presented by *Afonso et al.* [2008a], based on the simultaneous and self-consistent fitting of all the available geophysical and petrological/geochemical observations. Besides allowing for a better control of the lateral and vertical variations of the bulk properties, this method reduces the uncertainties associated with fitting each observable alone or in pairs, as commonly done in the literature. Here we provide instructions to the user and present some illustrative examples that highlight the main advantages of our approach in comparison to other currently available methods/codes. LitMod3D and detailed documentation can be downloaded from http://www.es.mq.edu.au/staff/Software1.htm (see auxiliary material).[1] We expect the code to be distributed through the Computational Infrastructure for Geodynamics (CIG, http://www.geodynamics.org).

2. Method and Numerical Implementation

[4] The general methodology used in LitMod3D has been discussed elsewhere [*Afonso et al.*, 2008a]. Here we give only a brief summary of the method and discuss in detail the new implementations relevant to LitMod3D.

[5] LitMod3D is a collection of FORTRAN subroutines and shell scripts organized in two modules: a forward calculation module (referred to as LITMOD3D_FOR) and an interactive interface module (referred to as LITMOD3D_INTF) used to visualize and modify data. Both modules run efficiently in either single- or multiple-processor computers and have been compiled in several Linux distributions (see LitMod3D README file at http://www.es.mq.edu.au/staff/Software1.htm for details). Sections 2.1–2.5 describe the general computation scheme performed by the forward module.

[1] Auxiliary materials are available in the HTML. doi:10.1029/2009GC002391.

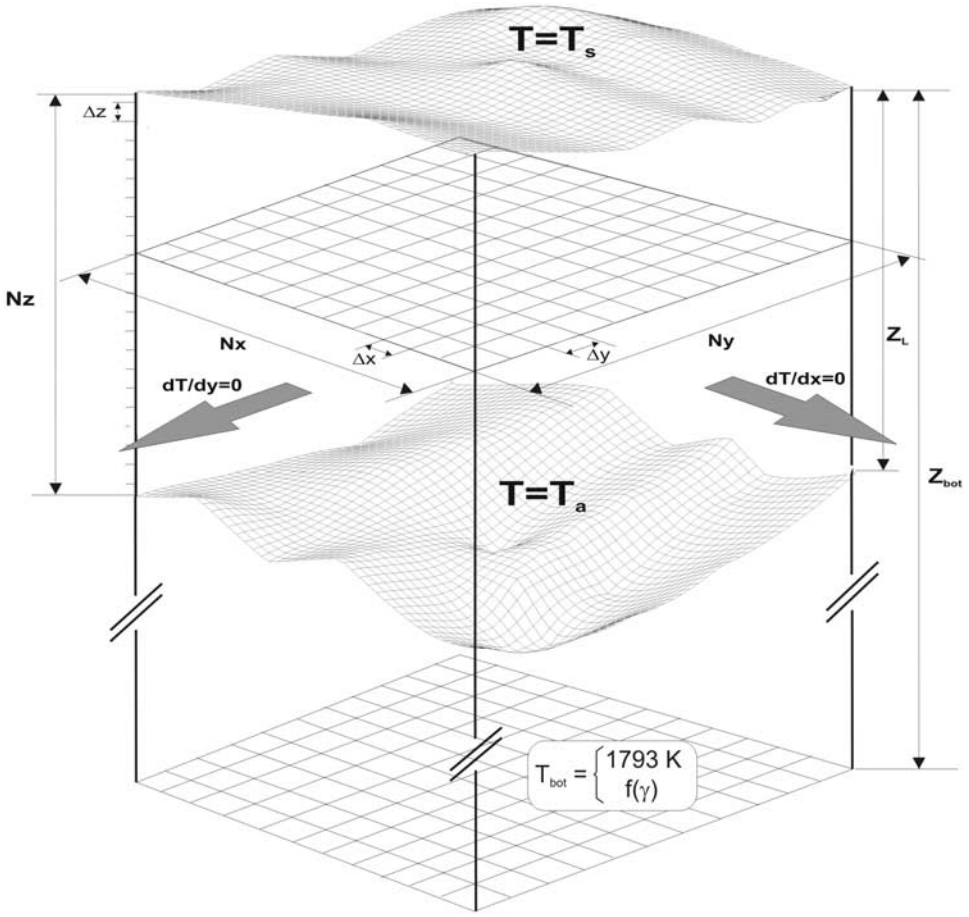

Figure 1. Scheme showing the main parameters of the FD grid and the boundary conditions used in LITMOD3D_FOR to solve the 3-D steady state heat transfer equation. See sections 2.1.1, 2.1.2, A1, and A2 for details.

2.1. Temperature

[6] For the calculation of the thermal field, LITMOD3D_FOR assumes the numerical domain to be composed of (1) a conduction-dominated region (i.e., lithosphere), (2) a convection-dominated region (i.e., convective sublithospheric upper mantle), and (3) an intermediate zone where both conduction and convection are significant [cf. *Afonso et al.*, 2008a].

2.1.1. Lithosphere

[7] In the absence of convection/advection terms, the 3-D steady state thermal structure of the lithosphere is given by the following vector equation

$$\nabla \cdot (k(\vec{x}, T, P)\nabla T(\vec{x})) = -H(\vec{x}) \qquad (1)$$

where T is temperature, k the thermal conductivity tensor (W m^{-1} K^{-1}), H the radiogenic heat production (W m^{-3}), and x denotes the spatial dependence. The temperature and pressure dependence of k in the mantle follows the model of *Hofmeister* [1999] (Appendix A1).

[8] Equation (1) is solved with the finite differences technique, subject to the following boundary conditions: (1) fixed temperature at the top (T_s) of the model, (2) fixed temperature at the bottom of the lithosphere (T_a), and (3) no heat flow perpendicular to the vertical boundaries (i.e., the four XZ and YZ planes, Figure 1).

2.1.2. Sublithospheric Mantle

[9] Heat transfer within the sublithospheric domain is dominated by convection [cf. *Schubert et al.*, 2001], and consequently, the temperature distribution follows approximately an adiabatic gradient. The bottom of the models is always taken at a depth z_{bot} = 400 km, where either a constant temperature or a range of adiabatic gradients can be chosen by the user (see Appendix A2). Between the lithosphere and sublithospheric mantle there is

Table 1. Estimates of Subcontinental Lithospheric Mantle Compositions From Xenoliths Suites and Peridotite Massifs[a]

Archons[b]	Average Archon Garnet SCLM[c]	Average Kaapvaal Harzburg	Average Slave Xenoliths	West Norway Average Dunite/Harzburg	East Greenland Average Xenoliths	Archon "Pristine" Estimate
SiO_2	45.7	45.9	42.9	42.9	43	42.7
TiO_2	0.04	0.05	0	0.01	0	0.01
Al_2O_3	0.99	1.3	1.1	0.21	0.45	0.4
Cr_2O_3	0.28	0.34	0.5	0.32	0.43	0.34
FeO	6.4	6.0	7.2	6.5	6.5	6.5
MnO	0.11	0.1	0.1	0.11	0.18	0.15
MgO	45.5	45.5	47.2	49.4	49	49.3
CaO	0.59	0.5	0.6	0.2	0.12	0.2
Na_2O	0.07	0.07	0.12	0.01	0.03	0.1
NiO	0.3	0.28	0.31	0.34	0.34	0.3
Mg #	92.7	93.1	92.1	93.1	93.1	93.1
Cr/(Cr + Al)	0.16	0.27	0.1	0.28	0.17	0.16

Protons[b]	Average Proton Garnet SCLM	Average Proton Xenoliths	Average Proterozoic Massif	Proton SCLM (Preferred)
SiO_2	44.7	43.9	45.2	44.6
TiO_2	0.09	0.04	0.09	0.07
Al_2O_3	2.1	1.6	2	1.9
Cr_2O_3	0.42	0.4	0.38	0.4
FeO	7.9	7.9	7.9	7.9
MnO	0.13	0.12	0.11	0.12
MgO	42.4	43.9	41.6	42.6
CaO	1.9	1.3	1.9	1.7
Na_2O	0.15	0.08	0.13	0.12
NiO	0.29	0.22	0.28	0.26
Mg #	90.6	90.8	90.4	90.6
Cr/(Cr + Al)	0.12	0.15	0.11	0.12

Tectons[b]	Average Tecton Garnet SCLM[c]	Average Tecton Garnet Peridotite	Average Spinel Peridotite	Average Tecton Peridotite	PUM MS[c,d]	PUM J79[d]
SiO_2	44.5	45	44	44.4	45	45.2
TiO_2	0.14	0.16	0.09	0.09	0.2	0.22
Al_2O_3	3.5	3.9	2.3	2.6	4.5	4
Cr_2O_3	0.4	0.41	0.39	0.4	0.38	0.46
FeO	8.0	8.1	8.4	8.2	8.1	7.8
MnO	0.13	0.07	0.14	0.13	0.14	0.13
MgO	39.8	38.7	41.4	41.1	37.8	38.3
CaO	3.1	3.2	2.2	2.5	3.6	3.5
Na_2O	0.24	0.28	0.24	0.18	0.36	0.33
NiO	0.26	0.24	0.26	0.27	0.25	0.27
Mg #	89.9	89.5	89.8	89.9	89.3	89.7
Cr/(Cr + Al)	0.07	0.07	0.1	0.09	0.05	0.07

[a] Modified from *Afonso et al.* [2008a] and *Griffin et al.* [2009].
[b] The nomenclature and classification of mantle domains used in Table 1 and in the text are those of *Griffin et al.* [1999] (modified from *Janse* [1994]).
[c] Compositions used in the models discussed in the text.
[d] PUM MS, primitive upper mantle composition of *McDonough and Sun* [1995]; PUM J79, primitive upper mantle composition of *Jagoutz et al.* [1979].

a "buffer" region with a continuous superadiabatic gradient where heat transfer is controlled by both conduction and convection (Appendix A2).

2.2. Thermodynamic Modeling and Bulk Properties

[10] In the mantle, stable mineral assemblages are computed by Gibbs free energy minimization

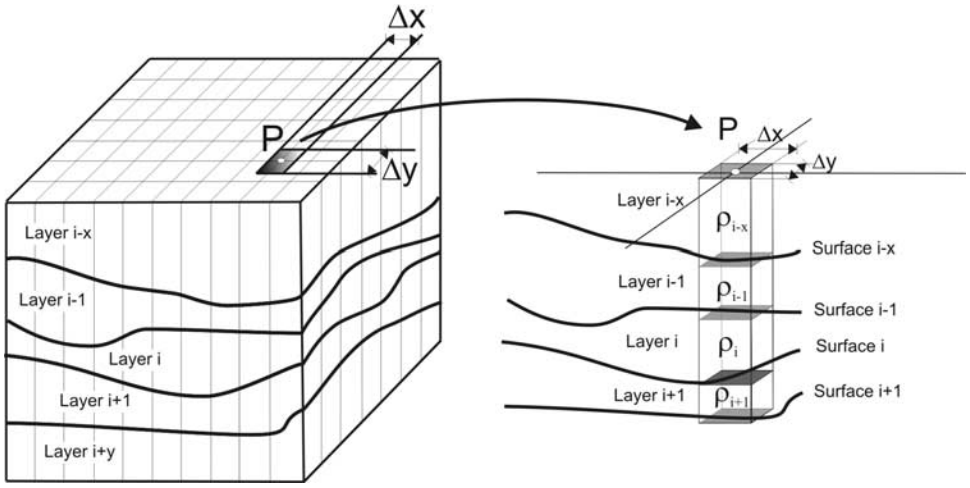

Figure 2. Schematic diagram showing the spatial transformation and subdivision of lithospheric columns into several vertical prisms centered on the grid nodes used in the computation of geoid and gravity anomalies.

[*Connolly*, 2005; *Afonso et al.*, 2008a]. Each mantle body is therefore characterized by a specific major element composition (in wt %), which translates into specific bulk rock properties. The latter are computed with a Voigt-Reuss-Hill averaging scheme. Table 1 summarizes typical average compositions of different subcontinental lithospheric domains estimated from xenoliths and peridotite massifs.

[11] The default thermodynamic formalism and associated database used in the free energy minimization are those of *Stixrude and Lithgow-Bertelloni* [2005]. However, other formalisms/databases [e.g., *Xu et al.*, 2008] can be easily implemented by slightly modifying the relevant subroutine of the forward module. All necessary files containing thermodynamic information can be generated either with the freely available software Perple_X (http://www.perplex.ethz.ch) [*Connolly*, 2005] or by using a simple interface provided with LitMod3D.

2.3. Pressure

[12] Density and pressure are coupled through the compressibility and the definition of lithostatic pressure $P(z)$

$$P(z) = \int_0^z \rho(z')g dz' \qquad (2)$$

In the crust, density is given by

$$\rho(T,P) = \rho_0 - \rho_0\alpha(T - T_0) + \rho_0\beta(P - P_0) \qquad (3)$$

where ρ_0 is a reference density at T_0 and P_0, α the coefficient of thermal expansion [K^{-1}], and β the compressibility [Pa^{-1}] (for layers with constant density both coefficients are zero). For mantle bodies, density is retrieved from the associated thermodynamic files as explained in section 2.2. The final pressure and density at each node are obtained through an iterative scheme as explained in Appendix B.

2.4. Elevation

[13] Local isostasy implies that a series of rigid vertical columns float freely on an inviscid fluid, and that the mass per unit area of these columns is the same at a certain level referred to as the compensation level [cf. *Turcotte and Schubert*, 2002]. If dynamic sublithospheric loads are neglected, then the compensation level can be placed at any depth below the base of the deepest lithospheric column [*Lachenbruch and Morgan*, 1990]. We take this level at the base of the numerical domain (i.e., 400 km) for the following reasons: (1) it covers the whole range of estimated lithospheric thicknesses and (2) a unique global compensation level requires only a single calibration constant (see Appendix C1 for the physical rationale behind this assumption).

[14] When short-wavelength (<200 km) density anomalies are present (e.g., intrusion), local isostasy is no longer valid to calculate elevation from the lithospheric geometry [cf. *Turcotte and Schubert*, 2002]. In these cases, LitMod3D accounts for the flexural rigidity of the lithosphere

(regional isostasy) by using a planform (2-D) elastic thin plate to calculate the vertical motions related to short-wavelength lithospheric loads (see details in Appendix C2).

2.5. Gravity and Geoid Anomalies

[15] Gravity and geoid anomalies are calculated in the spatial domain considering rectangular flat top prisms centered in each node of the grid (Figure 2). Although this approach is computationally more expensive than frequency domain techniques, it is better suited for handling density gradients and discontinuities within the model. The corresponding anomalies in every surface point of the model are calculated adding the effect of all individual prisms. The vertical gravitational attraction produced by a right rectangular prism whose density varies linearly with depth can be expressed analytically in Cartesian coordinates as [*Gallardo-Delgado et al.*, 2003]:

$$\begin{aligned}\Delta g_{FTP}(\rho) &= G\rho_0\left|\left|x\ln(y+r)+y\ln(x+r)-z\arctan\left(\frac{xy}{zr}\right)\right|_{x_1}^{x_2}\right|_{y_1}^{y_2}\Bigg|_{z_1}^{z_2}\\ &+G\gamma\left|\left|-xy\ln(r+z)-\frac{z^2}{2}\arctan\left(\frac{xy}{zr}\right)+\frac{x^2}{2}\arctan\left(\frac{yz}{xr}\right)+\frac{y^2}{2}\arctan\left(\frac{xz}{yr}\right)\right|_{x_1}^{x_2}\right|_{y_1}^{y_2}\Bigg|_{z_1}^{z_2}\\ r &= \sqrt{x^2+y^2+z^2}\\ \rho(z) &= \rho_0+\gamma z\\ G &= gravitational\ const.\left(6.6726\times10^{-11}m^3kg^{-1}s^{-2}\right)\end{aligned} \tag{4}$$

The first term on the right-hand side of equation (4) is equivalent to the contribution of a constant density prism [*Nagy et al.*, 2000]. The second term is related to the density gradient γ. Similarly, the corresponding geoid anomaly for the same prism is [*Fullea*, 2008]:

$$\begin{aligned}\Delta N_{FTP}(\rho) &= \frac{G\rho_0}{g}\left|\left|xy\ln(z+r)+yz\ln(x+r)+xz\ln(y+r)-P\right|_{x_1}^{x_2}\right|_{y_1}^{y_2}\Bigg|_{z_1}^{z_2}\\ &+\frac{G\gamma}{3g}\left|\left|xyr+\frac{y}{2}\left(y^2+3z^2\right)\ln(x+r)+\frac{x}{2}\left(x^2+3z^2\right)\ln(y+r)-z^3\arctan\left(\frac{xy}{zr}\right)\right|_{x_1}^{x_2}\right|_{y_1}^{y_2}\Bigg|_{z_1}^{z_2}\end{aligned} \tag{5}$$

where

$$P=\frac{z^2}{2}\arctan\left(\frac{xy}{zr}\right)+\frac{x^2}{2}\arctan\left(\frac{yz}{xr}\right)+\frac{y^2}{2}\arctan\left(\frac{xz}{yr}\right)$$

The Cartesian coordinates ($x_1 < x_2$, $y_1 < y_2$, z_1, z_2) define the prism dimensions and are referred to a coordinate system with its origin located at the point where the gravity/geoid anomaly is calculated. Details regarding the calculation procedure and numerical strategy are given in Appendix D.

3. Program Description

[16] LitMod3D considers every body of a model as a distinct layer. Each layer is characterized by its own set of physical properties (or bulk composition in mantle layers), and is defined between two consecutive and hierarchically ordered surfaces extended across the entire model (Figure 3). Calculations and outputs are referred to a Cartesian coordinate system with its origin located in the SW corner of the model. The shell script LITMOD3D.job centralizes all the input parameters and automatically generates the input files required by the two modules.

3.1. Forward Module: LITMOD3D_FOR

[17] Figure 4 (left) shows a general scheme of the files and folders used by LITMOD3D_FOR. The two input files LITMOD3D.info and layers.info contain all the parameters and variables needed by the forward module. LITMOD3D.info (generated by LITMOD3D.job) lists the following information on the geometry and boundary conditions of the model: (1) horizontal dimensions of the model L_x and L_y (km); (2) maximum topography of the region E_{max} (km); (3) number of nodes in the X, Y and Z axis, N_x, N_y, N_z; (4) vertical grid step Δz (km); (5) variable *topo*, which indicates whether the input topography has been smoothed (*topo* = 0) or not (*topo* = 1); (6) variable *temp_calc*, which indicates if temperature needs to be calculated (*temp_calc* = 1) or read from a file (*temp_calc* =

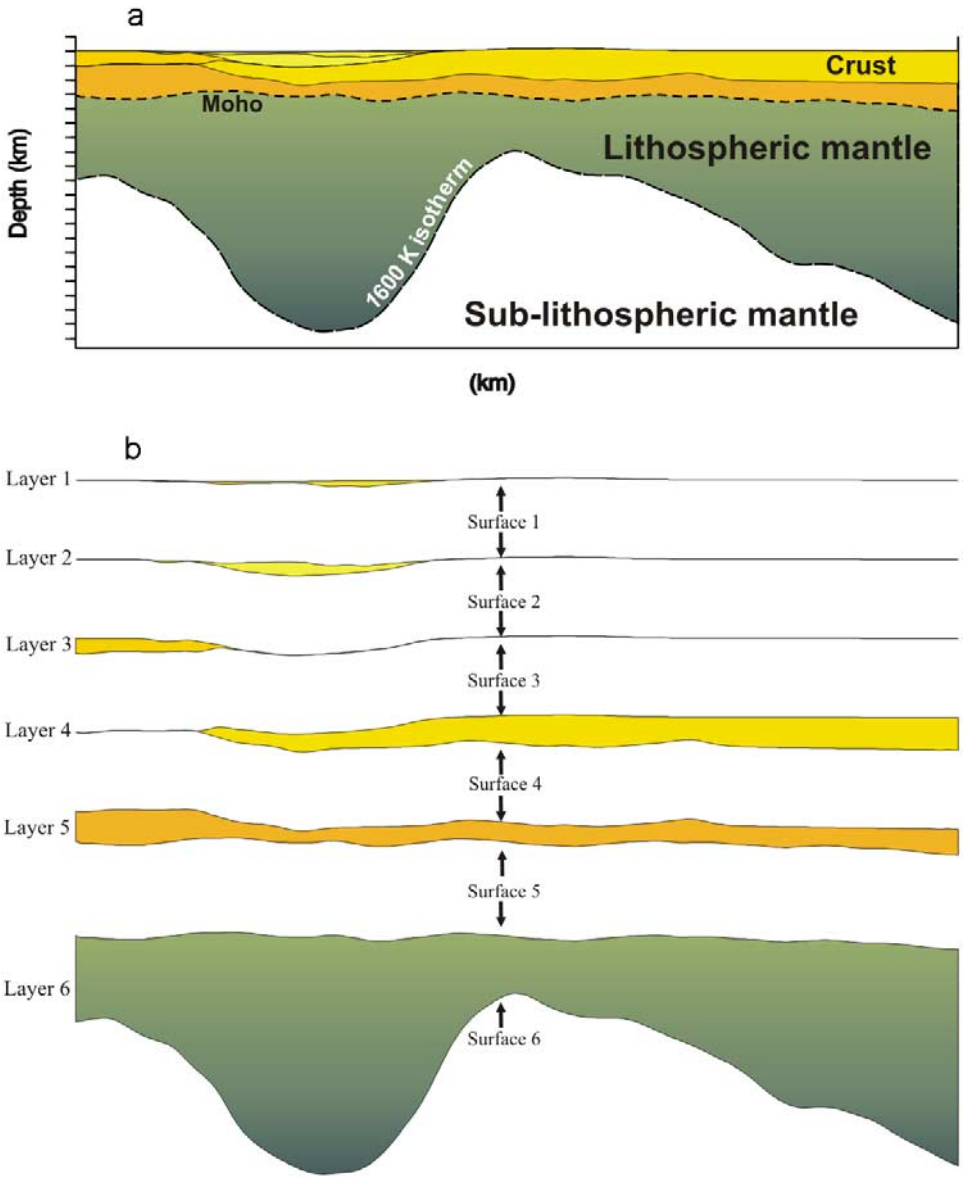

Figure 3. LitMod3D models are composed of a number of layers (bodies) with different physical properties, defined by an upper and a lower surface extended over the whole model. (a) Cross section of a lithospheric model. The color scale indicates different layers. (b) Detail of the layers and associated limiting surfaces. Each layer is defined by two consecutive surfaces (e.g., layer 3 is defined by its upper limit, surface 2, and its lower limit, surface 3). Note that each surface defines both the upper limit of an $(i + 1)$th layer and the lower limit of the ith layer.

0); and (7) fixed temperatures at the top and bottom of the lithosphere T_s and T_a, respectively.

[18] Each row in the input file layers.info corresponds to a specific layer (i.e., body) and contains the following information: (1) index number, (2) name/brief description, (3) reference density (STP conditions), (4) reference coefficient of thermal expansion (STP conditions), (5) thermal conductivity, (6) volumetric heat production term, (7) compressibility, (8) thermodynamic Grüneisen parameter, (9) pressure derivative of the isothermal bulk modulus, (10) isothermal bulk modulus, and (11) mantle reference number. Parameters 3 and 4 are referred to STP conditions. Parameters 8–11 are only relevant for mantle layers (see equation (A1)), whereas 3, 4, and 7 are only used in crustal layers. Parameter 11 is used to identify the composition of each mantle layer, and must be set to zero for crustal bodies. The folder mant_data (Figure 4, left) contains relevant thermodynamic information.

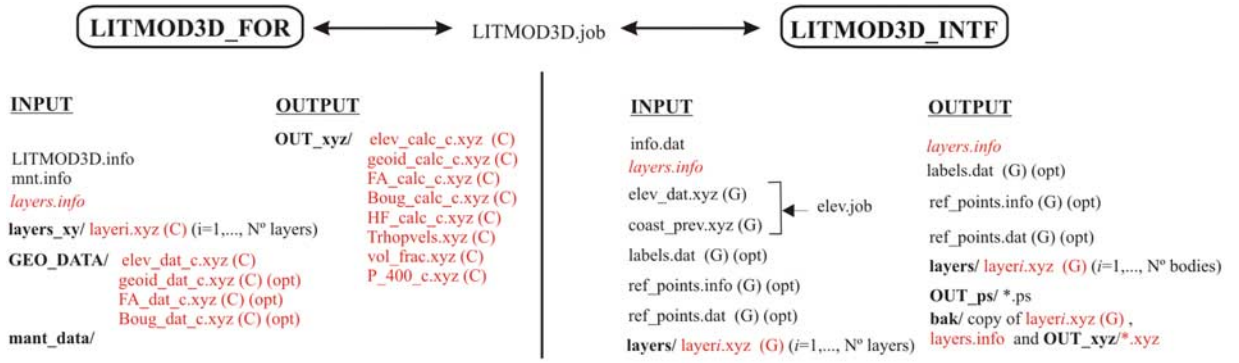

Figure 4. Scheme of the different input/output folders (in bold, followed by a slash) and files involved in (left) LITMOD3D_FOR and (right) LITMOD3D _INTF. Files and folders in red italics are shared by both LITMOD3D_FOR and LITMOD3D _INTF. After the name of the files, (C) means that the file is in Cartesian coordinates, whereas (G) indicates geographical coordinates. Files followed by (opt) are optional. See section 3 for further details.

3.2. Graphical Interface: LITMOD3D_INTF

[19] LITMOD3D_INTF is a graphical interface designed to visualize the outputs of LITMOD3D_FOR, handle input data, and modify the geometry and properties of the layers. It makes use of the freely available FORTRAN graphical libraries PGPLOT (http://www.astro.caltech.edu/~tjp/pgplot/). In contrast to LITMOD3D_FOR, LITMOD3D_INTF works in geographical coordinates. This makes easier the use and visualization of georeferenced input data. The shell script LITMOD3D.job automatically performs the required coordinate transformations in all the files shared by the two modules of LitMod3D. Figure 4 (right) shows the files and folders used by LITMOD_INTF.

[20] The main window of LITMOD3D_INTF (Figure 5a) shows map views of any of the available geophysical observables (right side of the window), together with general information on the model and an option menu (left side of the window). The observable displayed in map view (elevation by default) can be changed using the option CHANGE OBS (c).

[21] The options of the graphical interface can be classified in three general groups: visualization, modification, and additional data.

3.2.1. Visualization

[22] The program offers the following options to visualize the 3-D geometry of the model: (1) vertical cross sections of the structure and associated geophysical observables (EXTRACT PROFILE (p), Figures 5b and 5c); (2) map views of the structure, layer thickness, and observables (BODY PLOT (b, s), Figure 5d); and (3) vertical cross sections, map views (VISUALIZE (v), Figure 5e), and 1-D profiles (PROFILE (z), Figure 5f) of density, temperature, pressure and seismic velocity distributions.

3.2.2. Modification

[23] The geometry of the model is changed by modifying the boundary surfaces that define the layers. This is done along parallel profiles using the option MODIFY REGION (m). The selected surface appears as a dashed line in the profiles. A green line shows the last saved structure for comparison. After the profiles have been modified, the 3-D geometry is reconstructed by interpolating the structure between the saved profiles.

[24] The option ADD NEW LAYER (a) allows creating a new body by adding a new layer. The lateral distribution of the new layer is delineated by a number of closed polygons defined with the mouse over a map view of the model. The possi-

Figure 5. Different windows displayed by the graphical interface LITMOD3D_INTF. (a) Main window of LITMOD3D_INTF showing an elevation map of the study area. (b) Cross section displayed by the option EXTRACT PROFILE (p). Solid lines represent the geophysical observables calculated by LITMOD3D_FOR. Dashed lines indicate observed values. (c) The lithospheric geometry. (d) Thickness map of a particular layer. (e) Vertical profile showing the density variation with depth in a point of the model. (f) Horizontal slice showing the Vs velocity of the model at a certain depth.

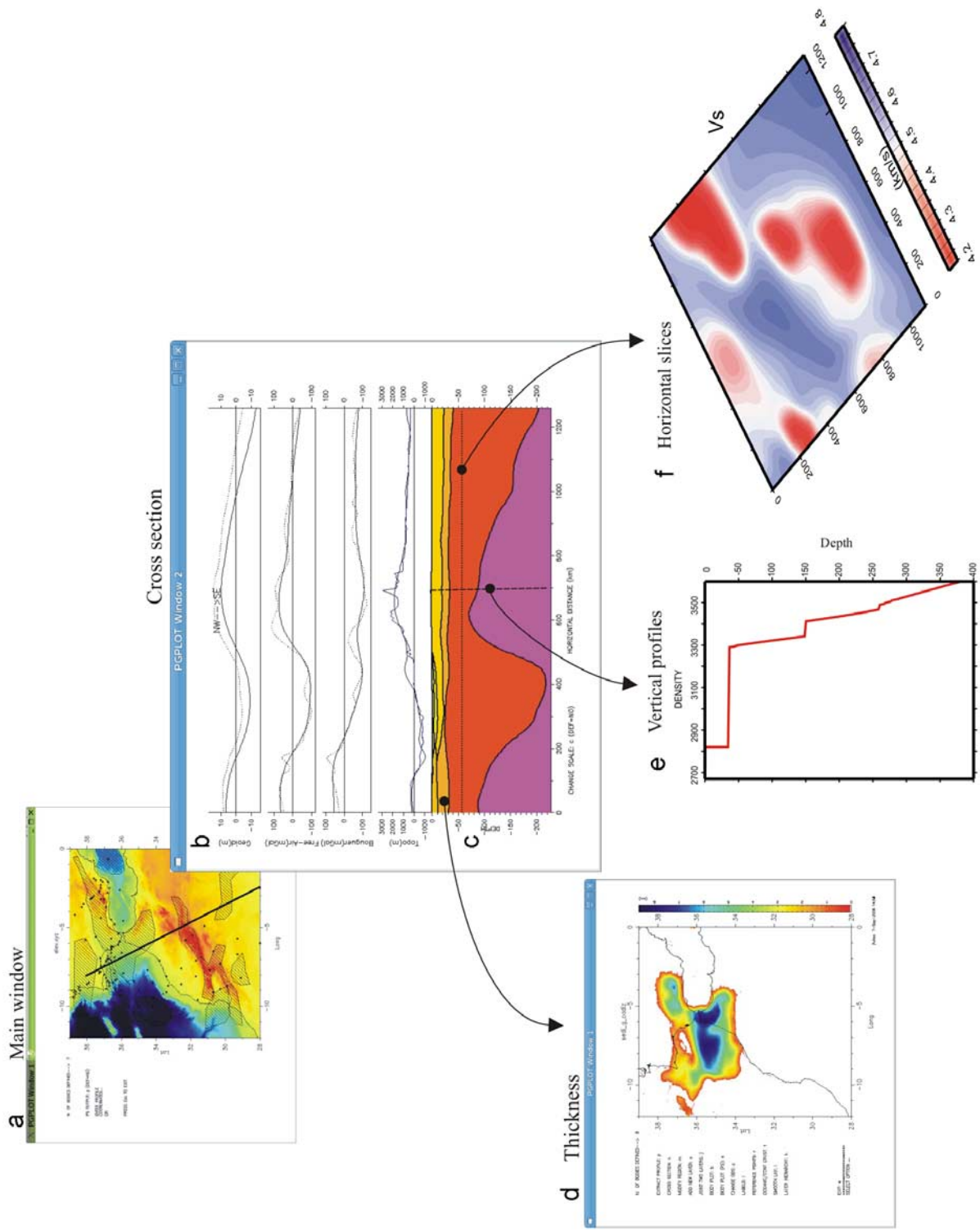
a Main window
Cross section
PGPLOT Window 2
b
c
d Thickness
e Vertical profiles
DENSITY
Depth
f Horizontal slices
Vs
(km/s)

Figure 5

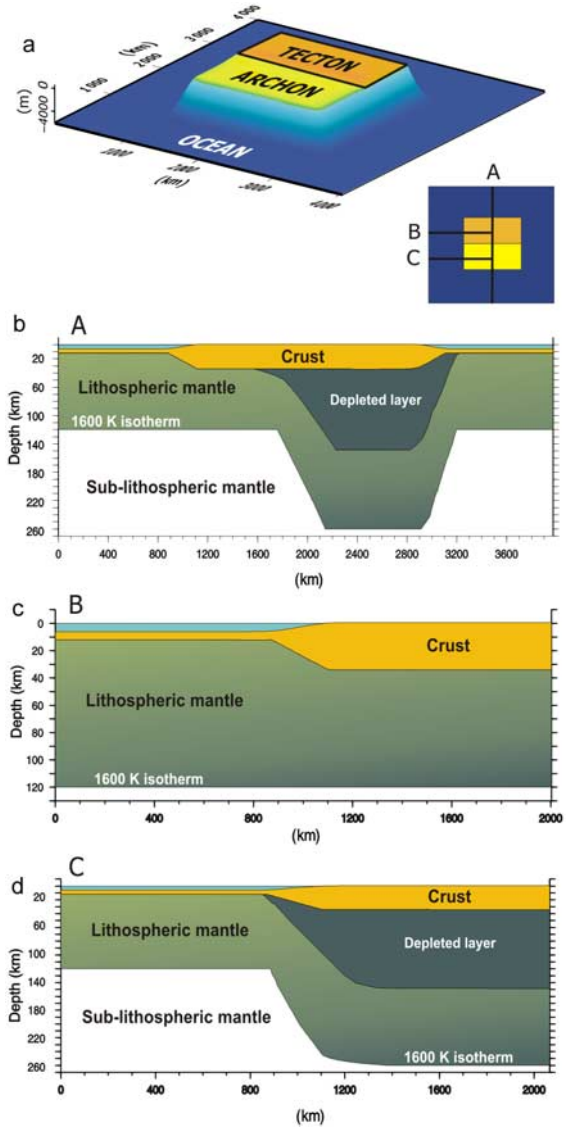

Figure 6. Synthetic model composed of three domains: "oceanic," Tecton, and Archon. The crust has a thickness of 35 km in the continental domain and 6.5 km in the oceanic domain and a constant density ρ_c = 2820 kg m^{-3} everywhere. These values are within common estimates for Precambrian and Paleozoic crust [*Durrheim and Mooney*, 1994; *Christensen and Mooney*, 1995]. The mantle beneath the ocean and Tecton domains is characterized by a typical Phanerozoic composition, whereas the Archon mantle composition displays the following stratification: Archean from the Moho to 150 km depth and Phanerozoic from 150 km to the base of the thermal lithosphere (Table 1). The entire model is in isostatic equilibrium. (a) Location of the three domains and cross sections. (b) Cross section A: the three domains. (c) Cross section B: the ocean and Tecton domains. (d) Cross section C: the ocean and Archon domains. Table 1 list the major element compositions (CFMAS) adopted for the mantle domains. Note that the scales in Figures 6b–6d are different.

bility to remove parts of a layer is available through the option JOIN TWO LAYERS (j). The option LAYER HIERARCHY (h) checks for the proper order between two surfaces, and makes corrections if necessary. A particular body can be completely removed by using DELETE LAYER (d). Finally, SMOOTH LAY (i) is a smoothing filter of surfaces.

3.2.3. Additional Data

[25] There are two additional data options: LABELS (l) and REFERENCE POINTS (r). The former allows introducing labels (i.e., text strings) with relevant information associated with locations of particular interest. The latter allows drawing a number of closed polygons (i.e., areas over a map view of the model) that would be projected in the main window. These options are intended to mark areas or bodies of particular relevance.

4. Illustrative Examples

[26] The examples in this section are intended to illustrate some of the functionalities of the code, as well as some of its advantages over other available modeling software. Although particular care has been taken to make these synthetic models realistic and useful, they are deliberately oversimplified and therefore the reader is urged to view them as a means of illustration only. In what follows we will focus on (1) the differences in the resulting temperature distribution when fitting the same geophysical observables with different methods and (2) the effect of including shallow phase transitions on the final lithospheric structure derived from gravity anomalies in thin crust scenarios (e.g., passive margins, intracontinental basins). In our comparison, we will consider only those methods that admit a temperature-dependent density (hereafter referred to as PTA approach) [e.g., *Zeyen and Fernàndez*, 1994; *Fullea et al.*, 2007]. Modeling techniques in which density is considered independent of T, P, or composition are not reliable and will not be examined here.

[27] To explore the two aforementioned effects we use a synthetic model composed of three lithospheric domains (Figure 6). The "oceanic" domain is characterized by a bathymetry of 6 km, a 6.5-km-thick crust, and a 120-km-thick lithospheric mantle. In the center of the model, there is a 2000 × 2000 km microcontinent with an elevation of 0.7 km above sea level. Its northern half is characterized by a typical Tecton structure and compo-

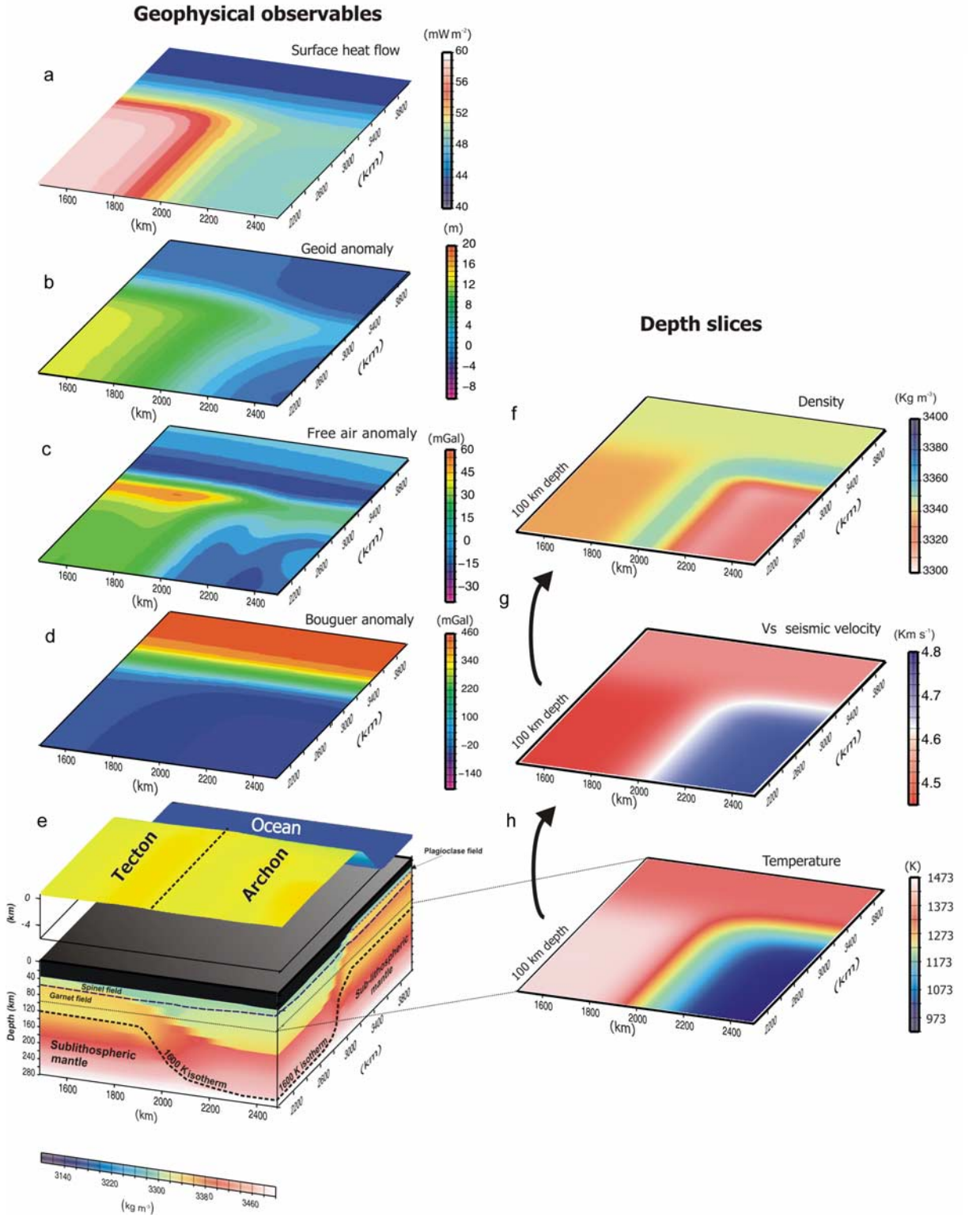

Figure 7. Modeling results for elevation, gravity, and geoid anomalies obtained with LitMod3D for the synthetic model of Figure 6. The lateral sides of the 3-D block show the density structure. The black dashed line represents the base of the thermal lithosphere (i.e., 1600 K isotherm). (a) Surface heat flow. Calculated (b) geoid, (c) free air, and (d) Bouguer anomalies. (e) The 3-D block. Depth slices of the (f) density, (g) Vs, and (h) thermal structures at a 100 km depth. Shown velocities are anharmonic isotropic velocities. However, LitMod3D includes the option to compute attenuation effects following the approach explained by *Afonso et al.* [2008a].

sition, whereas the southern half is representative of an Archon domain [*Afonso et al.*, 2008a; *Griffin et al.*, 2009]. Since we are particularly interested in the effects of sub-Moho features, we assign the same crustal structure for the two continental domains (Figure 6).

[28] The temperature field and associated geophysical observables of this synthetic model are shown in Figure 7. The variation pattern of these observables is controlled mainly by the lateral variation in crustal thickness (>20 km from "ocean" to Tecton). Note that the magnitude and pattern of the predicted observables are well within the range of real observations across passive margins [e.g., *Fernàndez et al.*, 2004]. The free-air and geoid anomalies do not change significantly in a transect running from the ocean to the Archon domain, indicating that the average density contrast between these two domains is small. This occurs because of the "light" Archean upper compositional layer, which counteracts the density increase associated with the cold thermal structure of this domain [*Jordan*, 1978; *Afonso et al.*, 2008a]. This is consistent with the weak correlation between the long-wavelength component of the gravity field and cratons [*Shapiro et al.*, 1999]. Conversely, the Bouguer anomaly exhibits an amplitude of about 470 mGal, reflecting mainly the effect of the Moho topography. The lithospheric thickening from the Tecton to the Archon domain reduces the surface heat flow by 10 mW m^{-2}, leading to a typical cratonic value of 48 mW m^{-2} [*Jaupart and Mareschal*, 1999] (Figure 7).

4.1. Comparison Between the PTA and LitMod3D

[29] The PTA assumes no explicit compositional variations within the mantle. The density of the lithosphere depends on temperature only (i.e., $\rho = \rho_a\,[1 + \alpha(T - T_a)]$), while the "asthenospheric density" ρ_a, coefficients of thermal expansion α, and thermal conductivities k, are assumed constant [e.g., *Lachenbruch and Morgan*, 1990; *Zeyen and Fernàndez*, 1994; *Fullea et al.*, 2007, and references therein]. This implies that mantle density reaches its highest value right beneath the Moho. However, as shown in section 4.2, this outcome produces artificial lateral density contrasts between the crust and the mantle that can significantly affect the modeling of gravity anomalies, besides being inconsistent with petrological and thermodynamic concepts.

[30] Predictions from the PTA for the same thermal and lithospheric structure of our LitMod3D synthetic model are shown in Figure 8. As expected, the calculated density structure displays a pronounced high-density region beneath the "cold" Archon, which translates into a large reduction of absolute elevation (>2 km of isostatic disequilibrium, Figure 8c). Likewise, and partly as a consequence of this disequilibrium, free-air and geoid anomalies are ~250 mGal and >100 m higher, respectively, in the PTA than in LitMod3D.

[31] Outside the Archon domain, differences in absolute elevations between the two models are significantly smaller (<300 m and <100 m in the Tecton and oceanic domains, respectively; Figures 7 and 8). This reflects the fact that the composition of the lithospheric mantle in these two domains is not too different from that in the sublithospheric counterpart (Table 1); an implicit assumption in the PTA. Gravity and geoid anomalies, on the other hand, are much more affected by the high-density root of the Archon. The effect is particularly evident in the geoid, which is more sensitive to long-wavelength deep-seated density anomalies than gravity anomalies.

[32] While the above results are revealing, it is more instructive to quantify the differences between the two methods in terms of the final lithospheric structure they predict. To do this, lets assume the geophysical observables predicted by LitMod3D to be the "real" data, and then use the PTA to obtain the lithospheric structure that best fits such data. For simplicity, we consider two end-member scenarios in which either the depth to the LAB or the crustal thickness is the only parameter allowed to vary.

[33] In the first case we find that fitting elevation requires a constant lithospheric thickness of 120 km throughout the model. This simple structure, however, is not able to simultaneously fit either the geoid or the surface heat flow in the Archon (Figure 7). In the second case, elevation, gravity, and geoid anomalies are fitted within 50 m, 5 mGal and 1 m, respectively, by increasing in 11 km the crustal thickness in the Archon (Figures 9b and 9c). Although the fitting of the observables is somewhat satisfactory, the predicted thermal structure and surface heat flow display localized differences of up to 200 K and 10 mW m^{-2}, respectively, compared to the thermal structure of LitMod3D (Figure 9d). Two different effects combine to produce this large difference in the Archon: (1) the thickening of the crust produces a "hotter" Archon

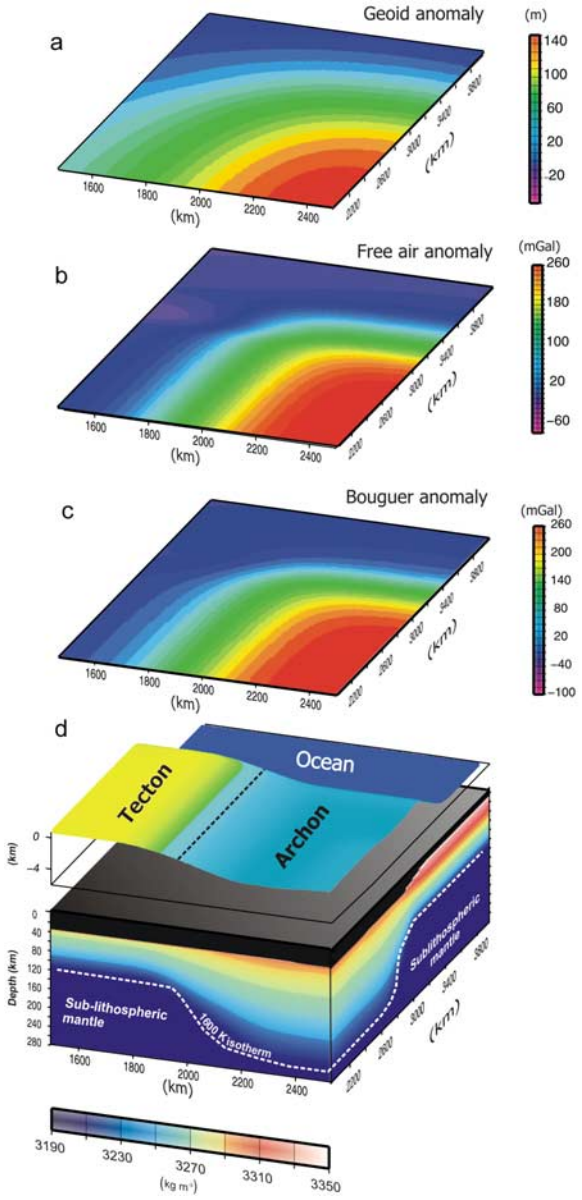

Figure 8. Modeling results for the (a) geoid, (b) free air, and (c) Bouguer anomalies computed using a temperature-dependent density in the lithospheric mantle and a constant density of 3200 kg m^{-3} in the sublithospheric mantle (see section 4.1 for further details). (d) The 3-D block with the calculated elevation on the top of it. The lateral sides of the 3-D block show the density structure. The white dashed line represents the base of the thermal lithosphere (i.e., 1600 K isotherm). Note that in comparison to the LitMod3D density distribution (see Figure 7), the mass excess beneath the Archon domain generates a prominent positive anomaly in all the potential fields and a decrease of elevation.

due to the larger radiogenic heat production of the crust and its relatively low thermal conductivity (blanketing effect; Figure 9) and (2) temperatures in the lithospheric mantle are higher in models with constant thermal conductivities (i.e., PTA). The first effect, required by the PTA to fit the observables, contributes the most to the final thermal difference (>80%) beneath the Archon.

4.2. Phase Transitions

[34] Two main phase transitions may occur within the lithospheric mantle: plagioclase-spinel (25–35

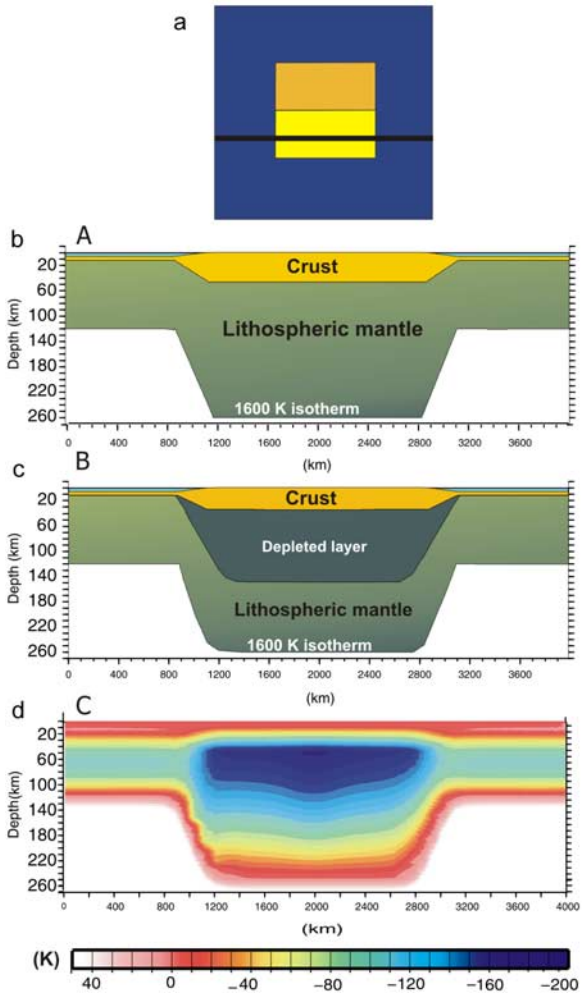

Figure 9. Comparison between the thermal fields calculated (1) using a model with constant thermal conductivity (k = 3.2 W m^{-1} K^{-1}) in which the density of the lithospheric mantle depends on temperature only (i.e., PTA) and (2) using the internally consistent approach of LitMod3D. Calculated geophysical observables are comparable in both cases (see the text for further details). (a) Location of profiles A, B, and C, which cut across the Archon domain. (b) Profile A: lithospheric structure of case 1. (c) Profile B: lithospheric structure of case 2. (d) Profile C: residual thermal structure obtained subtracting case 1 from 2. The large negative difference beneath the Archon is mainly the consequence of the different crustal structures predicted by the two models.

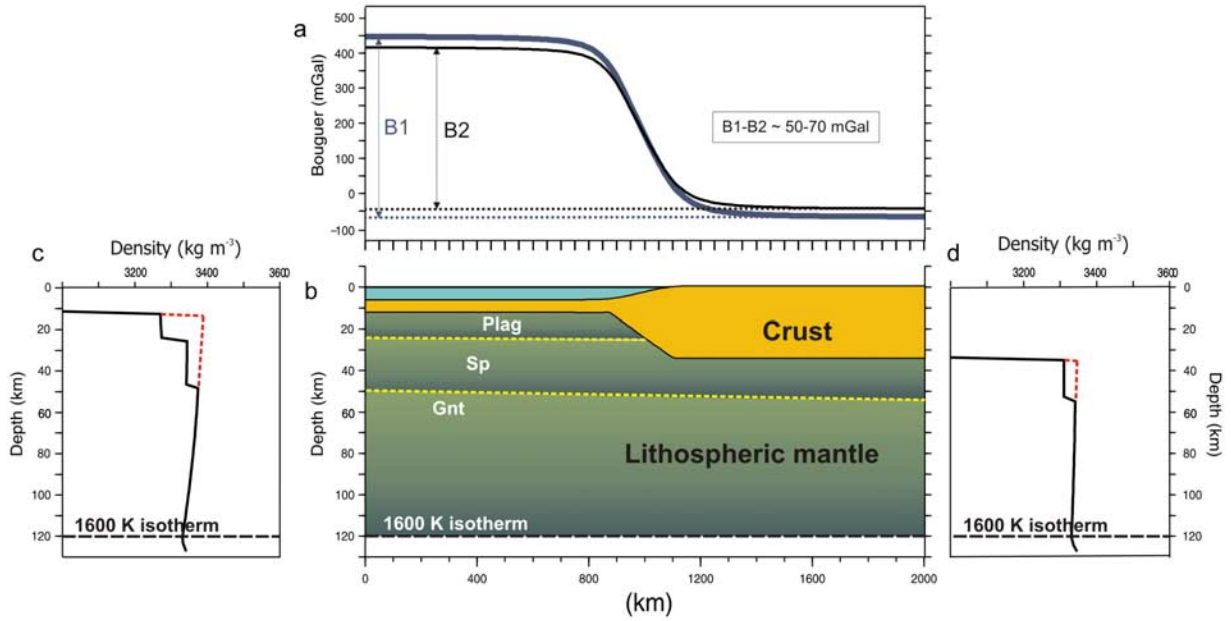

Figure 10. (a and b) Bouguer anomaly along a profile running from the ocean to the Tecton domain. Plag, plagioclase; Sp, spinel; Gnt, garnet. The density profiles (black lines) for (c) the ocean and (d) the Tecton domain. The red lines represent hypothetical density distributions in the case that the plagioclase-spinel and spinel-garnet phase transitions were removed. Note that while both plag-spinel and spinel-garnet phase transitions take place in the oceanic domain, only the latter is present in the Tecton because of its thicker crust. They also deepen toward the continent, where temperatures are higher because of the internal radioactive heat production of the crust.

km depth) and spinel-garnet (60–90 km depth) [*Ringwood*, 1975; *Klemme*, 2004]. Because (1) the density change associated with these phase transitions can be relatively large in fertile peridotites (<∼3% for plag-sp and <∼1.4% for sp-gnt [e.g., *Afonso et al.*, 2007; *Simon and Podladchikov*, 2008]) and (2) the transitions occur at relatively shallow depths, it is expected that they will influence the computation of gravity anomalies, particularly in settings characterized by a thin crust (e.g., intracontinental basins, passive margins, etc). However, this effect is routinely ignored in the modeling/interpretations of gravity anomalies. Relevant exceptions are the models of *Cella et al.* [1998, 2006], although their density computations and transition depths are not internally self-consistent.

[35] We quantify the impact of including/neglecting phase transitions by considering the resulting pattern of the Bouguer gravity anomaly along a transect running from the oceanic to the Tecton domain (Figure 10). We run two identical models hampering phase changes in one of them to retain only the effect of pressure and temperature on density. This is equivalent to what is assumed in the PTA method. As shown in Figure 10, we find that the effect of ignoring phase transitions in the computed gravity anomaly can be as large as 50–70 mGal, which is considered larger than typical uncertainties arising from internal density distributions within the crust. In order to make the patterns of Bouguer anomaly comparable in the two models, the one without phase transitions requires an oceanic crust 2–3 km thicker. It follows that neglecting phase stability in settings with pronounced crustal thinning can lead to errors up to ∼45% and ∼2% in the estimated crustal thickness and its internal density distribution, respectively.

Appendix A: Temperature Field

A1. Heat Transfer Equation

[36] The thermal conductivity $k(T, P)$ in the mantle is obtained from [*Hofmeister*, 1999]

$$k(T,P) = k_0\left(\frac{298}{T}\right)^a \exp\left(-(4\gamma + 1/3)\int_{298}^{T}\alpha(T)dT\right) \cdot \left(1 + \frac{K_0' P}{K_T}\right) + k_{rad}(T) \quad \text{(A1)}$$

where k_0 is the thermal conductivity at standard T-P conditions, a is a fitting parameter, γ is the thermodynamic/thermal Grüneisen parameter, α is

the T-dependent coefficient of thermal expansion, K_T is the isothermal bulk modulus, K'_0 its pressure derivative, and $k_{rad}(T)$ is a term that describes the radiation contribution to k (taken from *Hofmeister* [1999, equation (12)]). For typical mantle phases, the parameter a takes values between 0.2 and 0.9, while the Grüneisen parameter varies between 1.0 and 1.45 [*Hofmeister*, 1999]. We take the values of Forsterite (a = 0.45; γ = 1.25) as representative averages. The variation of k with composition in ultramafic assemblages is of the same order as variations produced by varying the individual parameters of equation (2) (k_0, a, γ, K'_0, K_T) within their uncertainties (including fabric anisotropy [e.g., *Gibert et al.*, 2003]). Therefore, we choose not to model k as an explicit function of bulk composition.

[37] LitMod3D uses a least squares iterative scheme to solve the linear system arising from the finite difference discretization of equation (1). The main reason for adopting an iterative method over a direct solver is computational speed. The coefficients in the linear system include k as a parameter, which is itself a function of T. This coupling is solved with an iterative procedure in which $k(T^{n-1})$ is updated in each iteration n. The iteration stops when a certain user-defined accuracy (strictly, a difference between T^n and T^{n-1}) is achieved. For accuracies <1°C, the system typically requires three to four iterations to converge.

A2. Sublithospheric and Superadiabatic Buffer Layers

[38] The region between the lithosphere and sublithospheric mantle where heat transfer is controlled by both conduction and convection is modeled with a buffer layer located immediately below the lithospheric domain. This buffer layer forces a continuous variation of temperature between the two domains and mimics the thermal effect of a rheologically active layer present at the bottom of the upper thermal boundary layer in convecting mantle-like fluids [*Solomatov and Moresi*, 2000; *Zaranek and Parmentier*, 2004]. In the buffer zone, the temperature varies linearly from the value at the bottom of the lithosphere (i.e., Ta = 1600 K) to T_{buffer} = 1673 K at the bottom of the buffer layer. In order to be consistent with both the adiabatic temperature profile at the reference MOR column [*Afonso et al.*, 2008a] and mantle convection models [*Solomatov and Moresi*, 2000; *Zaranek and Parmentier*, 2004; *Afonso et al.*, 2008b], the thickness of the buffer layer varies automatically to maintain the heat balance (i.e., energy conservation) between the basal heat input (assumed constant), internal heat generation, and surface heat release in the system.

[39] LitMod3D allows the user to define either a constant temperature at the bottom of the numerical domain T_{bot} or a range of adiabatic sublithospheric gradients. In the former case, an average reference temperature T_{bot} = 1793 K is recommended (default in LitMod3D). This estimation is based on high-pressure and high-temperature phase equilibrium experiments in the system $(Mg, Fe)_2SiO_4$ [e.g., *Frost*, 2003; *Katsura et al.*, 2004; *Frost and Dolejš*, 2007], and is consistent with estimations of (1) potential temperatures at mid-ocean ridges (MORs) and (2) the global average depth of the 410-km discontinuity [*Afonso et al.*, 2008a, and references therein]. Within the sublithospheric domain, the temperature (adiabatic) gradient is

$$\left.\frac{dT}{dz}\right|_{adiab} = \frac{T_{bot} - T_{buffer}}{z_{bot} - (z_L + z_{buffer})} \qquad \text{(A2)}$$

where z_L and z_{buffer} are the depths to the T_a and T_{buffer} isotherms, respectively. If T_{bot} is assumed constant (e.g., T_{bot} = 1793 K), then the sublithospheric gradient is univocally defined and varies laterally depending on the lithospheric structure. On the other hand, if a range of possible values for equation (A2) is defined, then T_{bot} will vary accordingly. The temperature gradient given by equation (A2) is allowed to vary only between the expected range of 0.35–0.6 K/km. This condition typically translates into maximum lateral temperature variations of ~120 K, in agreement with predictions from seismic observations on the topography of the 410-km discontinuity [e.g., *Afonso et al.*, 2008a; *Chambers et al.*, 2005, and references therein]. Note that if the chosen T_{bot} is considerably different from that listed above, then a new calibration constant need to be calculated for the elevation computation (see Appendix C).

Appendix B: First-Order Density-Pressure Iteration Formula

[40] In the crust, where the pressure effect is relatively small (see equation (3)), LitMod3D uses an explicit "one-iteration" formula derived as follows. Let us assume that the density $\rho(z_0)$ and pressure $P(z_0)$ at a certain depth z_0 are known. As a first estimate, we consider the following expression

for the pressure at a depth z > z_0 (z and z_0 belonging to the same material layer):

$$P(z) = P(z_0) + \rho(z_0) \cdot g \cdot (z - z_0) \tag{B1}$$

Equation (B1) is formally equivalent to assuming that the density in equation (2) is constant. In reality, density will change with pressure and temperature (equation (3)), and the resulting increase in pressure from z_0 to z is given, to first order, by the following integral

$$\begin{aligned}\Delta P &= \int_{z_0}^{z} \rho(z')g dz' = \int_{z_0}^{z} \rho_0\big(1 - \alpha\big(\overline{T} - T_0\big) + \beta(P(z_0) \\ &\quad + \rho(z_0)g \cdot (z' - z_0))\big)g dz' \\ &= \rho_0\big(1 - \alpha\big(\overline{T} - T_0\big) + \beta(P(z_0))g \\ &\quad \cdot (z - z_0) + \rho_0\beta\rho(z_0)g^2\frac{(z - z_0)^2}{2}\end{aligned} \tag{B2}$$

where T_0 and ρ_0 are the temperature and density at the surface, respectively. In equation (B2) we have assumed that the temperature variation between z and z_0 is linear, and therefore we can introduce the average value $\overline{T} = \frac{T(z) - T(z_0)}{2}$ in the integral. Equation (B2) can be rearranged to give

$$\begin{aligned}\Delta P &= \rho_0(1 - \alpha(T(z_0) - T_0) + \beta(P(z_0))g \cdot (z - z_0) \\ &\quad - \alpha\rho_0\left(\frac{T(z) - T(z_0)}{2}\right)g \cdot (z - z_0) \\ &\quad + \rho_0\beta\rho(z_0)g^2\frac{(z - z_0)^2}{2} \\ &= \left(\rho(z_0)\left(1 + \frac{\rho_0\beta g(z - z_0)}{2}\right) - \alpha\rho_0\left(\frac{T(z) - T(z_0)}{2}\right)\right)g \\ &\quad \cdot (z - z_0)\end{aligned} \tag{B3}$$

The first term within brackets on the right hand side of equation (B3) represents the first-order contribution (i.e., constant density) plus a correction term that depends on the compressibility and on the distance $z - z_0$. The second term within brackets accounts for the change in density due to the temperature difference between z and z_0. The total pressure at depth z is thus the sum of $P(z_0)$ plus ΔP, i.e., using differential notation:

$$\begin{aligned}P(z) = P(z - dz) + gdz\Bigg(&\rho(z - dz) \cdot \left(1 + \frac{g\rho_0\beta dz}{2}\right) \\ &-\rho_0\alpha\left(\frac{T(z) - T(z - dz)}{2}\right)\Bigg)\end{aligned} \tag{B4}$$

Equation (B4) can be introduced into equation (3) to obtain the density in the crust at any depth z provided that the pressure, density, and temperature are known at $(z - dz)$. At deeper levels, however, the accumulated error in calculated pressures can become substantial when using equation (B4). In this case, the pressure-density coupling is solved with a full iterative scheme. Iterations stop when the pressure difference between two consecutive iterations is less than a prescribed (user-defined) value.

Appendix C: Elevation, Compensation Level, and Regional Isostasy

C1. Compensation Level

[41] The application of hydrostatic equilibrium to the Earth's crust is one of the oldest physical principles in Earth Sciences and is commonly known as the principle of isostasy. Likewise, its extension to include the Earth's lithosphere [e.g., *Lachenbruch and Morgan*, 1990] may be referred to as lithospheric isostasy. The latter requires the mass per unit area of vertical lithospheric columns be the same when integrated down to a certain depth known as the compensation level. Although such condition is never met within the Earth, where convection currents occur, the relatively low viscosity of the shallow sublithospheric mantle allows lateral pressure gradients to be relaxed by flow over short time scales. In contrast, lateral pressure (and density) gradients associated with either temperature, topography, or compositional variations can exist within the lithosphere over much longer time scales. This creates a mechanical and temporal decoupling between the long-term rigid lithosphere and the much less viscous sublithospheric mantle [cf. *Schubert et al.*, 2001], which explains the success of lithospheric isostatic models [e.g., *Lachenbruch and Morgan*, 1990; *Zeyen and Fernandez*, 1994; *Fullea et al.*, 2007, and references therein] in reproducing absolute elevation.

[42] Several authors have demonstrated that the topography of the outer surface in mantle-like fluids is primarily controlled by the physical conditions within the uppermost thermal boundary layer [*McKenzie*, 1977; *Parsons and Daly*, 1983; *Marquart and Schmeling*, 1989]. Although "dynamic" loads associated with sublithospheric flow can influence the surface topography to some extent, this effect seems to be important only in regions of large upwellings or downwellings [e.g., *Marquart and Schmeling*, 1989]. In the isostatic balance performed in LitMod3D, the thermal gradient in the sublithospheric upper mantle does not include nonsteady thermal perturbations that could arise from convection currents, and therefore the

contribution of sublithospheric loads to elevation is implicitly neglected. This somehow limits the applicability of LitMod3D to regions presently affected by processes such as delamination or large upwellings. However, dynamic effects can be taken into account during the modeling process by properly correcting/filtering the input data.

[43] In the context of local isostasy the absolute elevation of any column is given by [*Afonso et al.*, 2008a]

$$E = L - \frac{P_{bot}}{g\rho_{bot}} - \prod_0 \quad if\ E > 0$$
$$E = \frac{\rho_{bot}}{\rho_{bot} - \rho_w}\left(L - \frac{P_{bot}}{g\rho_{bot}} - \prod_0\right) if\ E < 0 \qquad \text{(C1)}$$

where ρ_{bot} is the average density at the bottom of the model, ($z = z_{bot}$), P_{bot} the pressure at the bottom of each column, ρ_w the density of seawater (1030 kg m^{-3}), L is the solid part of each column (i.e., $L = z_{bot} + E_{obs}$ where E_{obs} is the observed elevation), and Π_0 is a calibration parameter depending on the reference column adopted. The latter can be calculated once a reference column is adopted. Following *Afonso et al.* [2008a], we take this reference column at a standard MOR. Using equation (C1) with appropriate parameters from the reference column, Π_0 is obtained as

$$\prod_0 = z_{bot} - \frac{\rho_{MOR}(z_{bot} - E_{rid}) + \rho_w E_{rid}}{\rho_{bot}} \qquad \text{(C2)}$$

where ρ_{MOR} and E_{rid} are the average density and average bathymetry, respectively, of the reference MOR column. Note that ρ_{MOR} and ρ_{bot} depend on the MOR model, and therefore on the assumed basal temperature T_{bot}. If the chosen T_{bot} is different from the default value of 1793 K (see above), a new calibration constant should be calculated accordingly as explained by *Afonso et al.* [2008a].

[44] Equations (C1) and (C2) are strictly valid for a flat Earth model. However, the differences with respect to a spherical Earth model, which allows for the change in the surface area with depth [e.g., *Hager*, 1983], are only relevant for very thick lithospheres. For instance, for a 200-km-thick lithosphere, the discrepancy in predicted elevations between spherical and flat Earth models is less than 5%.

C2. Regional Isostasy

[45] The presence of short-wavelength features in the density distribution can lead to unrealistic elevations and associated gravity anomalies under the assumption of local isostasy. In such cases, a regional (flexural) isostasy model may be more appropriate [*Turcotte and Schubert*, 2002].

[46] The equation relating the vertical deflection $w(x, y)$ of an elastic thin plate when submitted to vertical forces $q(x, y)$ [e.g., *van Wees and Cloetingh*, 1994] is:

$$\begin{aligned} &D\frac{\partial^4 w}{\partial x^4} + D\frac{\partial^4 w}{\partial y^4} + 2D\frac{\partial^4 w}{\partial x^2 \partial y^2} \\ &\quad + 2\frac{\partial D}{\partial x}\frac{\partial^3 w}{\partial x^3} + 2\frac{\partial D}{\partial y}\frac{\partial^3 w}{\partial y^3} + \frac{\partial^2 D}{\partial x^2}\frac{\partial^2 w}{\partial x^2} + \frac{\partial^2 D}{\partial y^2}\frac{\partial^2 w}{\partial y^2} \\ &\quad + \nu\frac{\partial^2 D}{\partial y^2}\frac{\partial^2 w}{\partial x^2} + \nu\frac{\partial^2 D}{\partial x^2}\frac{\partial^2 w}{\partial y^2} + 2\frac{\partial D}{\partial x}\frac{\partial^3 w}{\partial x \partial y^2} + 2\frac{\partial D}{\partial y}\frac{\partial^3 w}{\partial y \partial x^2} \\ &\quad + 2(1-\nu)\frac{\partial^2 D}{\partial x \partial y}\frac{\partial^2 w}{\partial x \partial y} \\ &\quad + \Delta\rho g\ w = q(x,y) \end{aligned} \qquad \text{(C3)}$$

where D is the rigidity of the lithosphere, w is the flexural deflection (vertical displacement), $\Delta\rho$ is the density difference between sublithospheric mantle and the overlying fluid (air or water), and $q(x, y)$ is the vertical pressure anomaly at the compensation level. Rigidity and the equivalent elastic thickness of the lithosphere *Te* are related according to the equation

$$D(x,y) = \frac{ET_e^3(x,y)}{12(1-\nu^2)} \qquad \text{(C4)}$$

where E is Young's Modulus ($E = 10^{11}$ Pa) and ν the Poisson's ratio ($\nu = 0.25$).

[47] Regional compensation reduces the deviations between compensated and observed elevations depending on the chosen *Te* values. Small *Te* values filter only short-wavelength misfits, and in the limit case of *Te* = 0, regionally and locally compensated elevation are identical (i.e., 100% compensation). On the other hand, large *Te* values filter both short- and long-wavelength misfits, and in the limit case of infinite *Te*, all loads are supported by the intrinsic rigidity of the lithosphere (i.e., 0% compensation). For example, a *Te* of 10 km and 30 km removes 16% and 84%, respectively, of the vertical displacement produced by a 200-km wavelength density anomaly with respect to predictions from local isostasy. This allows discerning whether low-wavelength misfits between the observed topography and the local isostatic topography compensating the assumed lithospheric structure can be due to a regional isostatic support assuming reasonable *Te* values.

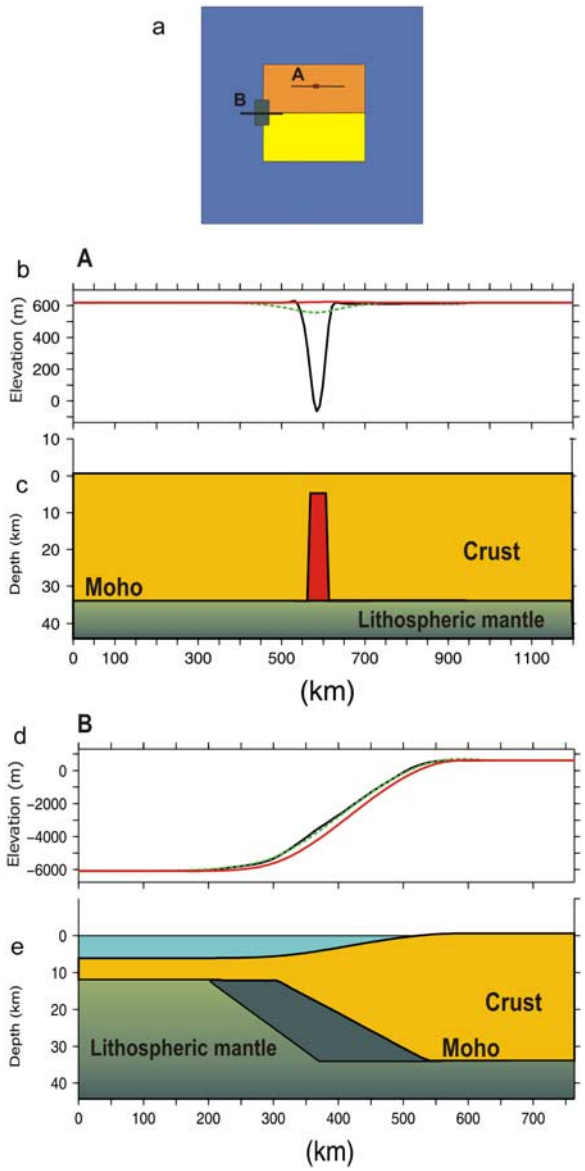

Figure C1. Differences between local and regional isostasy for two extra bodies. (a) Locations of cross sections A and B. (b and c) Cross section A: narrow structure of about 50 km width with its base located at the Moho, a vertical extension of 30 km, and a density contrast with respect to the surrounding crust of +70 kg m^{-3}. (d and e) Cross section B: body located right beneath the Moho extending 350 km and 600 km in the E–W and N–S directions, respectively, and with a maximum thickness of 20 km. The density contrast with respect to the surrounding mantle ranges from −70 to −150 kg m^{-3}. Figures C1c and C1e depict the geometry of the bodies, and Figures C1b and C1d show three elevation values: "observed" (red solid line), calculated according to local isostasy (black solid line), and calculated according to regional isostasy (green dashed line). For the flexural calculations, an elastic thickness of 30 km has been used.

[48] LitMod3D computes flexural isostasy by using the finite difference code TISC (cuba.ija.csic.es/~danielgc/tisc/) [*Garcia-Castellanos*, 2002], which requires the 2-D load distribution and a representative effective elastic thickness for the lithosphere. The flexural load $q(x, y)$ is given by pressure variations at the compensation level. Since sublithospheric loads are implicitly ignored (see above), these pressure variations are associated with lithospheric loads only. Therefore, in the ideal case where the observed topography and the modeled lithospheric structure are 100% locally compensated, the pressure at 400 km depth would be constant throughout the entire model and the load distribution would be zero.

[49] We illustrate the effect of regional compensation by introducing two new bodies in the Tecton area, which originally is 100% compensated (i.e., the calculated elevation according to local isostasy coincides with the input "observed" elevation). The first body is a 50 × 50 km wide body with its base located at the Moho, and a vertical extension of 30 km (Figures C1b and C1c). The density contrast with respect to the surrounding crust is +70 kg m^{-3}. This case is representative of a mafic intrusive body of small dimensions such as those found in many volcanic settings (e.g., Namibian volcanic margin [*Bauer et al.*, 2000; *Fernàndez et al.*, 2008]). The second body is located right beneath the Moho in the transition region between the oceanic and Tecton domains (Figures C1d and C1e). Its dimensions are 350 km × 600 km in the E–W and N–S directions, respectively, and its maximum thickness is 20 km. The density of this body is 3200 kg m^{-3}, which translates into a density contrast ranging from −70 to −150 kg m^{-3} with respect to the surrounding mantle. This body may well represent underplating material such as those typically found in volcanic margins (e.g., North Atlantic, Namibian margin [*White et al.*, 2008; *Fernàndez et al.*, 2004; *Bauer et al.*, 2000]).

[50] The presence of these two extra bodies introduces misfits between the "observed" elevation (see above) and that predicted by local isostasy. The misfits are attenuated by accounting for the flexural strength of the lithosphere, depending on the assumed effective elastic thickness and on the wavelength of the load. For instance, assuming a Te = 30 km, the flexural resistance reduces about 90% of the misfit between observed and calculated elevations (in local isostasy) for the first body, but only <10% for the second (Figure C1). This simple

exercise demonstrates the well-known fact that for structures extending for more than about 200–250 km, local isostasy is a reasonable approximation [cf. *Turcotte and Schubert*, 2002].

Appendix D: Gravity and Geoid Anomalies

[51] Equations (4) and (5) are solved using absolute densities. However, since only relative gravity and geoid anomalies are meaningful in the present context, the gravity field of a reference model is subtracted from the total field. The free air gravity anomaly is therefore given directly by the gravitational attraction of equation (4) minus the effect of the reference model. Bouguer gravity anomalies are obtained by correcting free air anomalies for the gravitational attraction of topography assuming constant reduction densities of 2670 kg/m^3 and 1030 kg/m^3 for the crust and water, respectively. Although there are no global data sets of Bouguer gravity anomalies, it is straightforward to calculate Bouguer gravity anomalies from global digital free-air anomaly data sets by applying the complete topography correction [see *Fullea et al.*, 2008].

[52] Columns located at the edges of the model are extended 10^6 km to avoid border effects produced by the density contrasts at the physical limits of the model. The average of the calculated gravity anomalies is fit to coincide with the average of the observed anomalies. In the case of geoid anomalies, long-wavelength (regional) components are usually present in the observed signal because of their slower decay ($\sim$1/r) with distance to density anomalies. Moreover, small perturbations from isostatic equilibrium (local or flexural) at the borders of the model can result in long-wavelength components in the calculated anomaly. These undesirable effects are removed by subtracting from the calculated geoid the planes that best fit (in a least squares sense) the observed and calculated geoid anomalies [*Fullea*, 2008]. When comparing predictions with real geoid data, it is crucial to properly filter the data to avoid undesirable deep convective effects. In most cases, this can be achieved to a good approximation by removing harmonic coefficients up to degree and order 9–10 from a complete undulation model (see *Bowin* [1983], *Torne et al.* [1995], and *Bowin* [2000] for a more complete discussion).

[53] In order to use equations (4) and (5), the density of each prism needs to be either constant or vary linearly with depth. In the crust, this condition is always met to a high accuracy, and therefore the top and bottom surfaces of each crustal layer are used to define the vertical limits of the prisms. Within the mantle, on the other hand, density can vary nonlinearly or abruptly within a single layer (e.g., across phase changes). To account for this, LITMOD3D_FOR performs three hierarchically ordered subdivisions. First, one prism is defined for each mantle layer (as for the crust). Second, the program searches for possible phase transitions within each layer, defining one prism for each stability field. Third, a further check is performed to corroborate that the density at the middle of each prism is close enough to the average between the values at its upper and lower boundaries (i.e., difference smaller than a user-defined error). If this condition is not met, the prism is subdivided until the third condition is met. In practice, tests for different mantle compositions and lithospheric geometries suggest that a single iteration suffices.

Acknowledgments

[54] This work was supported by the Spanish research projects 01-LEC-EMA22F-EUROMARGINS-ESF, CTM2005-08071-C03-03/MAR, and Consolider TopoIberia CSD2006-00041 (J.F., J.C.A., and M.F.). We thank Generic Mapping Tools (GMT) and PGPLOT developers for making their tools available to the community and S. Zlotnik for his advice on numerical matters. We are also grateful for helpful reviews from D. Schutt, C. Lithgow-Bertelloni, and J. Gaherty. This is contribution 605 from the Australian Research Council National Key Centre for the Geochemical Evolution and Metallogeny of Continents (http://www.es.mq.edu.au/GEMOC).

References

Afonso, J. C., G. Ranalli, and M. Fernàndez (2007), Density structure and buoyancy of the oceanic lithosphere revisited, *Geophys. Res. Lett.*, *34*, L10302, doi:10.1029/2007GL029515.

Afonso, J. C., M. Fernàndez, G. Ranalli, W. L. Griffin, and J. A. D. Connolly (2008a), Integrated geophysical-petrological modeling of the lithosphere and sublithospheric upper mantle: Methodology and applications, *Geochem. Geophys. Geosyst.*, *9*, Q05008, doi:10.1029/2007GC001834.

Afonso, J. C., S. Zlotnik, and M. Fernàndez (2008b), Effects of compositional and rheological stratifications on small-scale convection under the oceans: Implications for the thickness of oceanic lithosphere and seafloor flattening, *Geophys. Res. Lett.*, *35*, L20308, doi:10.1029/2008GL035419.

Bauer, K., S. Neben, B. Schreckenberger, R. Emmermann, K. Hinz, N. Fechner, K. Gohl, A. Schulze, R. B. Trumbull, and K. Weber (2000), Deep structure of the Namibia continental margin as derived from integrated geophysical studies, *J. Geophys. Res.*, *105*, 25,829–25,853, doi:10.1029/2000JB900227.

Bowin, C. (1983), Depth of principal mass anomalies contributing to the Earth's Geoidal Undulations and gravity anomalies, *Mar. Geod.*, *7*, 61–100, doi:10.1080/15210608309379476.

Bowin, C. (2000), Mass anomalies and the structure of the Earth, *Phys. Chem. Earth*, *25*(4), 343–353, doi:10.1016/S1464-1895(00)00056-9.

Carlson, R. W., D. G. Pearson, and D. E. James (2005), Physical, chemical, and chronological characteristics of continental mantle, *Rev. Geophys.*, *43*, RG1001, doi:10.1029/2004RG000156.

Cella, F., F. Fedi, G. Florio, and A. Rapolla (1998), Gravity modelling of the litho–asthenosphere system in the central Mediterranean, *Tectonophysics*, *287*, 117–138, doi:10.1016/S0040-1951(98)80064-4.

Cella, F., S. Lorenzo, M. Fedi, M. Loddo, F. Mongelli, A. Rapolla, and G. Zito (2006), Temperature and density of the Tyrrhenian lithosphere and slab and new interpretation of gravity field in the Tyrrhenian Basin, *Tectonophysics*, *412*, 27–47, doi:10.1016/j.tecto.2005.08.025.

Chambers, K., J. H. Woodhouse, and A. Deuss (2005), Topography of the 410-km discontinuity from PP and SS precursors, *Earth Planet. Sci. Lett.*, *235*, 610–622, doi:10.1016/j.epsl.2005.05.014.

Christensen, N. I., and W. D. Mooney (1995), Seismic velocity structure and composition of the continental crust: A global view, *J. Geophys. Res.*, *100*, 9761–9788, doi:10.1029/95JB00259.

Connolly, J. A. D. (2005), Computation of phase equilibria by linear programming: A tool for geodynamic modeling and its application to subduction zone decarbonation, *Earth Planet. Sci. Lett.*, *236*, 524–541, doi:10.1016/j.epsl.2005.04.033.

Durrheim, R. J., and W. D. Mooney (1994), Evolution of the Precambrian lithosphere: Seismological and geophysical constraints, *J. Geophys. Res.*, *99*, 15,359–15,374, doi:10.1029/94JB00138.

Fernàndez, M., I. Marzán, and M. Torné (2004), Lithospheric transition from the Variscan Iberian Massif to the Jurassic oceanic crust of the central Atlantic, *Tectonophysics*, *386*, 97–115, doi:10.1016/j.tecto.2004.05.005.

Fernàndez, M., J. C. Afonso, and G. Ranalli (2008), The deep lithospheric structure of the Namibian volcanic margin, *Tectonophysics*, doi:10.1016/j.tecto.2009.02.036, in press.

Fouch, M. J., P. G. Silver, D. R. Bell, and J. N. Lee (2004), Small-scale variations in seismic anisotropy near Kimberley, South Africa, *Geophys. J. Int.*, *157*, 764–774, doi:10.1111/j.1365-246X.2004.02234.x.

Frost, D. J. (2003), The structure and sharpness of $(Mg,Fe)_2SiO_4$ phase transformations in the transition zone, *Earth Planet. Sci. Lett.*, *216*, 313–328, doi:10.1016/S0012-821X(03)00533-8.

Frost, D. J., and D. Dolejš (2007), Experimental determination of the effect of H_2O on the 410-km seismic discontinuity, *Earth Planet. Sci. Lett.*, *256*, 182–195, doi:10.1016/j.epsl.2007.01.023.

Fullea, J. (2008), Development of numerical methods to determine the lithospheric structure combining geopotential, lithostatic and heat transport equations. Application to the Gibraltar arc system, Ph.D. thesis, Univ. de Barcelona, Barcelona, Spain.

Fullea, J., M. Fernàndez, H. Zeyen, and J. Vergés (2007), A rapid method to map the crustal and lithospheric thickness using elevation, geoid anomaly and thermal analysis. Application to the Gibraltar Arc System and adjacent zones, *Tectonophysics*, *430*, 97–117, doi:10.1016/j.tecto.2006.11.003.

Fullea, J., M. Fernàndez, and H. Zeyen (2008), FA2BOUG—A FORTRAN 90 code to compute Bouguer gravity anomalies from gridded free air anomalies: Application to the Atlantic-Mediterranean transition zone, *Comput. Geosci.*, *34*, 1665–1681, doi:10.1016/j.cageo.2008.02.018.

Gallardo-Delgado, L. A., M. A. Pérez-Flores, and E. Gómez-Treviño (2003), A versatile algorithm for joint 3D inversion of gravity and magnetic data, *Geophysics*, *68*, 949–959, doi:10.1190/1.1581067.

Garcia-Castellanos, D. (2002), Interplay between lithospheric flexure and river transport in foreland basins, *Basin Res.*, *14*(2), 89–104, doi:10.1046/j.1365-2117.2002.00174.x.

Gibert, B., U. Seipold, A. Tommasi, and D. Mainprice (2003), Thermal diffusivity of upper mantle rocks: Influence of temperature, pressure, and the deformation fabric, *J. Geophys. Res.*, *108*(B8), 2359, doi:10.1029/2002JB002108.

Griffin, W. L., S. Y. O'Reilly, and C. G. Ryan (1999), The composition and origin of sub-continental lithospheric mantle, in *Mantle Petrology: Field Observations and High-Pressure Experimentation: A Tribute to Francis R. (Joe) Boyd*, edited by Y. Fei, C. M. Berkta, and B. O. Mysen, *Spec. Publ. Geochem. Soc.*, *6*, 13–45.

Griffin, W. L., S. O'Reilly, J. C. Afonso, and G. C. Begg (2009), The composition and evolution of lithospheric mantle: A re-evaluation and its tectonic implications, *J. Petrol.*, doi:10.1093/petrology/egn033, in press.

Hager, B. H. (1983), Global isostatic geoid anomalies for plate and boundary layer models of the lithosphere, *Earth Planet. Sci. Lett.*, *63*, 97–109, doi:10.1016/0012-821X(83)90025-0.

Hofmeister, A. M. (1999), Mantle values of thermal conductivity and the geotherm from phonon life times, *Science*, *283*, 1699–1706.

Jagoutz, E., H. Palme, H. Baddenhausen, K. Blum, M. Cendales, G. Dreibus, B. Spettel, V. Lorenz, and H. Wanke (1979), The abundance of major, minor and trace elements in the Earth's mantle as derived from primitive ultramafic nodules, *Geochim. Cosmochim. Acta*, *2*, suppl. 2031–2050.

Janse, A. J. A. (1994), Is Clifford's Rule still valid? Affirmative examples from around the world, in *Diamond: Characterization, Genesis and Exploration*, edited by H. O. A. Meyer and O. Leonardos, *CPRM Spec. Publ.*, vol. 1A/93, pp. 215–235, Co. de Pesqui. de Recursos Minerais, Rio de Janeiro, Brazil.

Jaupart, C., and J. C. Mareschal (1999), The thermal structure and thickness of continental roots, *Lithos*, *48*, 93–114, doi:10.1016/S0024-4937(99)00023-7.

Jordan, T. H. (1978), Composition and development of the continental tectosphere, *Nature*, *274*, 544–548.

Katsura, T., et al. (2004), Olivine-wadsleyite transition in the system $(Mg, Fe)_2SiO_4$, *J. Geophys. Res.*, *109*, B02209, doi:10.1029/2003JB002438.

Klemme, S. (2004), The influence of Cr on the garnet-spinel transition in the Earth's mantle: Experiments in the system MgO-Cr_2O_3-SiO_2 and thermodynamic modelling, *Lithos*, *777*, 639–646.

Lachenbruch, A. H., and P. Morgan (1990), Continental extension, magmatism and elevation; formal relations and rules of thumb, *Tectonophysics*, *174*, 39–62, doi:10.1016/0040-1951(90)90383-J.

Levshin, A. L., J. Schweitzer, C. Weidle, N. M. Shapiro, and M. H. Ritzwoller (2007), Surface wave tomography of the Barents Sea and surrounding regions, *Geophys. J. Int.*, *170*, 441–459, doi:10.1111/j.1365-246X.2006.03285.x.

Marquart, G., and H. Schmeling (1989), Topography and geoid undulations caused by small scale convection beneath continental lithosphere of variable elastic thickness, *Geophys. J. Int.*, *97*, 511–527, doi:10.1111/j.1365-246X.1989.tb00520.x.

McDonough, W. F., and S.-S. Sun (1995), The composition of the Earth, *Chem. Geol.*, *120*, 223–253, doi:10.1016/0009-2541(94)00140-4.

McKenzie, D. (1977), Surface deformation, gravity anomalies and convection, *Geophys. J. R. Astron. Soc.*, *48*, 211–238.

Nagy, D., G. Papp, and J. Benedek (2000), The gravitational potential and its derivatives for the prism, *J. Geod.*, *74*, 552–560, doi:10.1007/s001900000116.

Parsons, B., and S. Daly (1983), The relationship between surface topography, gravity anomalies, and the temperature structure of convection, *J. Geophys. Res.*, *88*, 1129–1144, doi:10.1029/JB088iB02p01129.

Ringwood, A. E. (1975), *Composition and Petrology of the Earth's Mantle*, McGraw-Hill, New York.

Schubert, G., D. L. Turcotte, and P. Olson (2001), *Mantle Convection in the Earth and Planets*, 940 pp., Cambridge Univ. Press, Cambridge, U. K.

Shapiro, S. S., B. H. Hager, and T. H. Jordan (1999), The continental tectosphere and Earth's long-wavelength gravity field, *Lithos*, *48*, 135–152.

Shomali, Z. H., R. G. Roberts, L. B. Pedersen, and the TOR Working Group (2006), Lithospheric structure of the Tornquist Zone resolved by nonlinear P and S teleseismic tomography along the TOR array, *Tectonophysics*, *416*, 133–149, doi:10.1016/j.tecto.2005.11.019.

Simon, N. S. C., and Y. Y. Podladchikov (2008), The effect of mantle composition on density in the extending lithosphere, *Earth Planet. Sci. Lett.*, *272*, 148–157, doi:10.1016/j.epsl.2008.04.027.

Solomatov, V. S., and L. Moresi (2000), Scaling of time-dependent stagnant lid convection: Application to small-scale convection on the Earth and other terrestrial planets, *J. Geophys. Res.*, *105*, 21,795–21,818, doi:10.1029/2000JB900197.

Stixrude, L., and C. Lithgow-Bertelloni (2005), Mineralogy and elasticity of the oceanic upper mantle: Origin of the low-velocity zone, *J. Geophys. Res.*, *110*, B03204, doi:10.1029/2004JB002965.

Torne, M., M. Fernàndez, J. Carbonell, and E. Banda (1995), Lithospheric transition from continental to oceanic in the West Iberia Atlantic Margin, in *Rifted Ocean-Continent Boundaries*, edited by E. Banda, M. Torne, and M. Talwani, pp. 247–263, Kluwer Acad., Dordrecht, Netherlands.

Turcotte, D. L., and G. Schubert (2002), *Geodynamics*, 2nd ed., 456 pp., Cambridge Univ. Press, Cambridge, U. K.

van Wees, J. D., and S. Cloetingh (1994), A finite difference technique to incorporate spatial variation in rigidity and planar faults into 3D models for lithospheric flexure, *Geophys. J. Int.*, *117*, 179–196, doi:10.1111/j.1365-246X.1994.tb03311.x.

White, R. S., L. K. Smith, A. W. Roberts, P. A. F. Christie, N. J. Kusznir, and the rest of the iSIMM Team (2008), Lower-crustal intrusion on the North Atlantic continental margin, *Nature*, *452*, 460–464, doi:10.1038/nature06687.

Xu, W., C. Lithgow-Bertelloni, L. Stixrude, and J. Ritsema (2008), The effect of bulk composition and temperature on mantle seismic structure, *Earth Planet. Sci. Lett.*, *275*, 70–79, doi:10.1016/j.epsl.2008.08.012.

Zaranek, S. E., and E. M. Parmentier (2004), The onset of convection in fluids with strongly temperature-dependent viscosity cooled from above with implications for planetary lithospheres, *Earth Planet. Sci. Lett.*, *224*, 371–386, doi:10.1016/j.epsl.2004.05.013.

Zeyen, H., and M. Fernàndez (1994), Integrated lithospheric modeling combining thermal, gravity, and local isostasy analysis: Application to the NE Spanish Geotransect, *J. Geophys. Res.*, *99*, 18,089–18,102, doi:10.1029/94JB00898.